Measurement of the Generalized Polarizabilities of the Proton in Virtual Compton Scattering

Proposal to Jefferson Lab PAC-43

H. Atac, A. Blomberg, S. Joosten, Z.E. Meziani,
M. Paolone (spokesperson), N. Sparveris (spokesperson / contact person)
Temple University, Philadelphia, PA, USA

A. Camsonne (spokesperson), J.P. Chen, M. Jones (spokesperson)
Thomas Jefferson National Accelerator Facility, Newport News, VA, USA

T. Badman, S. Li, E. Long, K. McCarty, C. Meditz, M. O'Meara, R. Paremuzyan, S. Santiesteban, P. Solvignon-Slifer, K. Slifer, B. Yale, R. Zielinski
University of New Hampshire, Durham NH, 03824

K. Allada, A. Bernstein, S. Gilad
Massachusetts Institute of Technology, Cambridge, MA, USA

E. Cline, R. Gilman, A. Tadepalli
Rutgers, The State University of New Jersey, Piscataway, New Jersey 08854, USA

Z. Zhao
Duke University, Durham, NC, USA

X. Bai, D. Di, K. Gnanvo, C. Gu, N. Liyanage, H. Nguyen
University of Virginia, Charlottesville, VA, US

B. Dongwi, N. Kalantarians, M. Kohl, A. Liyanage, J. Nazeer, A. Nuruzzaman
Hampton University, Hampton, Virginia 23668, USA

S. Bae, S. Choi, J. Ha
Seoul National University, Department of Physics & Astronomy, Seoul 151-747 Korea

P. Markowitz
Florida International University, Miami, Florida 33199, USA

J. Beričič, T. Brecelj, S. Širca, S. Štajner
Jožef Stefan Institute and Faculty of Mathematics and Physics, University of Ljubljana, Slovenia

H. Fonvieille
Clermont Université, UBP, CNRS-IN2P3, LPC, BP 10448, F-63000 Clermont-Ferrand, France

C.E. Hyde
Department of Physics, Old Dominion University, Norfolk VA 23529

A. Asaturyan, A. Mkrtchyan, H. Mkrtchyan, V. Tadevosyan, S. Zhamkochyan
I. A. Alikhanian National Science Laboratory (Yerevan Physics Institute), Yerevan, Armenia

V. Punjabi
Norfolk State Univeristy, Norfolk VA 23504

C. F. Perdrisat
The College of William and Mary, Williamsburg VA

A.T. Katramatou, G.G. Petratos
Kent State University, Kent, OH 44242

D. Androic
University of Zagreb, Physics Department, Bijenicka 32, HR-10000 Zagreb

M. Elsaar
Southern University at New Orleans, New Orleans, LA 70126

B. Pasquini
Dipartimento di Fisica, Universita' degli Studi di Pavia, and Istituto Nazionale di Fisica Nucleare, Sezione di Pavia, Pavia, Italy

G. Huber
University of Regina, Regina, SK S4S0A2, Canada

W. Armstrong
Argonne National Laboratory, Argonne, IL

(Dated: May 16, 2015)

Abstract

We propose to conduct a measurement of the Virtual Compton Scattering reaction in Hall C that will allow the extraction of the two scalar Generalized Polarizabilities of the proton in the region of $Q^2 = 0.4$ $(GeV/c)^2$ to $Q^2 = 0.75$ $(GeV/c)^2$. The Generalized Polarizabilities are fundamental quantities of the nucleon, sensitive to both the role of the quark and pion degrees of freedom, and as such they are extremely valuable for a deeper and more complete understanding of the nucleon structure. The unique capabilities of Hall C, namely the high resolution of the spectrometers combined with the ability to place the spectrometers in small angles, will provide high precision measurements that will allow to explore the mechanisms responsible for the non-trivial Q^2 dependence of α_E, will significantly improve the knowledge of β_M, and will contribute in a valuable way to our understanding of the nucleon dynamics. The experimental setup utilizes standard Hall C equipment, namely the HMS and SHMS spectrometers and a 15 cm liquid hydrogen target. A total of 14 days of unpolarized 85 μA electron beam with energy of 4400 MeV is requested for this experiment.

I. INTRODUCTION

The proposed experiment offers to explore the scalar Generalized Polarizabilities of the proton through measurements of the Virtual Compton Scattering reaction in Hall C. The experiment will offer high precision measurements of α_E and β_M in the region of $Q^2 = 0.4$ $(GeV/c)^2$ to $Q^2 = 0.75$ $(GeV/c)^2$. These measurements will contribute significantly to a more complete understanding of the nucleon dynamics. A brief introduction on the Generalized Polarizabilities will be followed by a detailed discussion on the physics goals of the proposal, the design of the experiment and the expected measurements.

A. The Generalized Polarizabilities of the Proton

The polarizabilities of a composite system such as the nucleon are elementary structure constants, just as its size and shape, and can be accessed experimentally by Compton scattering processes. In the case of real Compton scattering (RCS), the incoming real photon deforms the nucleon, and by measuring the energy and angular distributions of the outgoing photon one can determine the induced current and magnetization densities. The global strength of these densities is characterized by the nucleon polarizabilities. In contrast, the virtual Compton scattering (VCS) process is obtained if the incident real photon is replaced by a virtual photon. The virtuality of the photon allows us to map out the spatial distribution of the polarization densities. In this case it is the momentum of the outgoing real photon q' that defines the size of the perturbation while the momentum of the virtual photon q sets the scale of the observation. In analogy to the form factors for elastic scattering, which describe the charge and magnetization distributions, VCS gives access to the deformation of these distributions under the influence of an electromagnetic field perturbation as a function of the distance scale. The structure dependent part of the process is parametrized by the Generalized Polarizabilities (GPs).

The GPs are fundamental quantities of the nucleon, sensitive to both the role of the quark and pion degrees of freedom and as such they are extremely valuable for a deeper and more complete understanding of the nucleon structure. They can be seen as Fourier transforms of local polarization densities (electric, magnetic, and spin) and therefore are a probe of the nucleon dynamics, allowing us, e.g., to study the role of the pion cloud and quark core contributions to the nucleon GPs at various length scales. They depend on the quantum numbers of the two electromagnetic transitions involved in the Compton process and typically a multipole notation is adopted. Initially ten independent lowest-order GPs were defined [1]; it was shown [2, 3] that nucleon crossing and charge conjugation symmetry reduce this number to six, two scalar (S=0) and four spin, or vector GPs (S=1). They can be defined as shown in table I. The two scalar GPs, electric and magnetic, are defined as:

$$\begin{aligned} \alpha_E(Q^2) &= -P^{(L1,L1)0}(Q^2) \cdot (\tfrac{e^2}{4\pi}\sqrt{\tfrac{3}{2}}) \\ \beta_M(Q^2) &= -P^{(M1,M1)0}(Q^2) \cdot (\tfrac{e^2}{4\pi}\sqrt{\tfrac{3}{8}}) \end{aligned}$$

The electric and the magnetic GPs(Q^2) are an extension of the well known static electric α_E and magnetic β_M polarizabilities obtained in real Compton scattering [4]. Contrary to the form factors that describe only the ground state of the nucleon, the polarizabilities are sensitive to all the excited spectrum of the nucleon. One can offer a very naive picture of the polarizabilities which are the resulting effect of an electromagnetic perturbation applied to the nucleon components. For example, an electric field moves positive and negative charges inside the proton in opposite directions. The

TABLE I: Notation for the six dipole GPs. In the first column the notation uses the polarization state $\rho(\rho')$ of the initial (final) photon, the angular momentum $L(L')$ of the transition, and the non spin-flip ($S = 0$) or spin-flip ($S = 1$) of the nucleon. The multipole notation in the second column uses the magnetic and longitudinal multipoles. The six listed GPs correspond to the lowest possible order in q'_{cm}, i.e. a dipole final transition ($l' = 1$). The third column gives the correspondence in the RCS limit, defined by $Q^2 \to 0$ or $q_{cm} \to 0$.

$P^{(\rho' L', \rho L)S}(q_{cm})$	$P^{(f,i)S}(q_{cm})$	RCS limit
$P^{(01,01)0}$	$P^{(L1,L1)0}$	$-\frac{4\pi}{e^2}\sqrt{\frac{2}{3}}\ \alpha_E$
$P^{(11,11)0}$	$P^{(M1,M1)0}$	$-\frac{4\pi}{e^2}\sqrt{\frac{8}{3}}\ \beta_M$
$P^{(01,01)1}$	$P^{(L1,L1)1}$	0
$P^{(11,11)1}$	$P^{(M1,M1)1}$	0
$P^{(01,12)1}$	$P^{(L1,M2)1}$	$-\frac{4\pi}{e^2}\frac{\sqrt{2}}{3}\ \gamma_3$
$P^{(11,02)1}$	$P^{(M1,L2)1}$	$-\frac{4\pi}{e^2}\frac{2\sqrt{2}}{3\sqrt{3}}(\gamma_2+\gamma_4)$

induced electric dipole moment is proportional to the electric field, and the proportionality coefficient is the electric polarizability which measures the rigidity of the proton. On the other hand, a magnetic field acts differently on the quarks and the pion cloud giving rise to two different contributions, a paramagnetic and a diamagnetic, to the magnetic polarizability. Contrary to atomic polarizabilities, which are of the size of the atomic volume, the proton electric polarizability α_E [4] is much smaller than the volume scale of a nucleon (only a few % of its volume). The small size of the polarizabilities reveals the extreme stiffness of the proton as a direct consequence of the strong binding of its inner constituents, the quarks and gluons, while representing a natural indication of the intrinsic relativistic character of the nucleon. In most theoretical models the electric GP α_E is predicted to decrease monotonically with Q^2. The smallness of the magnetic GP β_M relative to α_E can be explained by the existence of the competing paramagnetic and diamagnetic contributions, which nearly cancel. Furthermore, the β_M is predicted to go through a maximum before decreasing. This last feature is usually explained by the dominance of diamagnetism due to the pion cloud at long distance, or small Q^2, and the dominance of paramagnetism due to a quark core at short distance (large Q^2).

B. Virtual Compton Scattering and the GPs

One can explore the GPs through VCS which is accessed experimentally by exclusive photon electroproduction as shown in Figure 1. Kinematics are defined by five independent variables, the incoming and final electron energies, the scattered electron angle, and the polar and azimuthal angles of the Compton subprocess in its center-of-mass. Due to electron scattering, one also has the Bethe-Heitler process (BH) where the final photon is emitted by the incoming or outgoing electron. The photon electroproduction amplitude is the coherent sum of the Bethe-Heitler, Born and non-Born contributions as shown in Figure 2. The (BH) and (Born) parts, produced due to bremsstrahlung of the electron or proton, respectively, are well known and are entirely calculable, with the nucleon EM form factors as inputs, while the non-Born amplitude contains the dynamical internal structure information in terms of GPs.

The LET (Low energy theorem) [1] provides a path to access these observables analytically. According to the LET, or LEX (Low-energy EXpansion), the amplitude $T^{ep\gamma}$ is expanded in powers of q'_{cm}. As a result, the (unpolarised) $ep \to ep\gamma$ cross section at small q'_{cm} can be written as:

$$d^5\sigma \;=\; d^5\sigma^{BH+Born} \;+\; q'_{cm}\cdot\phi\cdot\Psi_0 \;+\; \mathcal{O}(q'^2_{cm}) \tag{1}$$

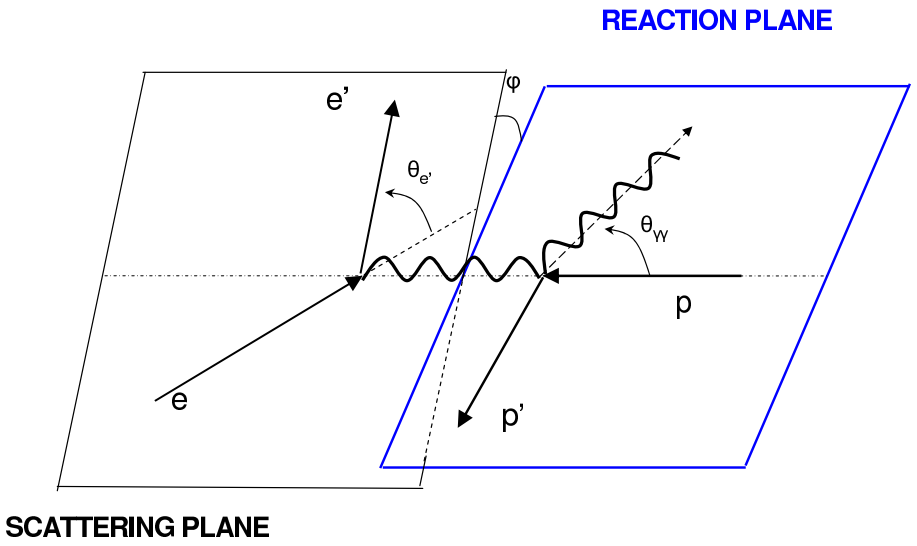

FIG. 1: The Virtual Compton Scattering reaction

where ϕ is a phase-space factor. The notation $d^5\sigma$ stands for $d^5\sigma/dk'_{elab}d\Omega'_{elab}d\Omega_{cm}$ where k'_{elab} is the scattered electron momentum in the lab frame, $d\Omega'_{elab}$ its solid angle in the lab frame and $d\Omega_{\gamma cm}$ the solid angle of the outgoing photon (or proton) in the p-γ^* CM frame. The Ψ_0 term comes from the interference between the Non-Born and the BH+Born amplitudes at lowest order in q'_{cm}; it gives the leading polarizability effect in the cross section. The LET approach is valid only below the pion production threshold, i.e. as long as the Non-Born amplitude remains real.

The Ψ_0 term contains three structure functions P_{LL}, P_{TT} and P_{LT}:

$$\Psi_0 \;=\; v_1 \cdot (P_{LL} - \frac{1}{\epsilon} P_{TT}) \;+\; v_2 \cdot P_{LT} \tag{2}$$

where ϵ is the usual virtual photon polarisation parameter and v_1, v_2 are kinematical coefficients depending on $(q_{cm}, \epsilon, \theta_{cm}, \varphi)$. θ_{cm} and φ are the polar and azimuthal angles of the Compton scattering process in the CM frame of the initial proton and virtual photon (Fig. 1). The full expression of v_1, v_2 can be found in ref [1], as well as the expression of the structure functions versus the GPs. For the structure functions one has:

$$\begin{aligned} P_{LL} &= \tfrac{4M}{\alpha_{em}} \cdot G_E^p(Q^2) \cdot \alpha_E(Q^2) \\ P_{TT} &= [P_{TT\ spin}] \\ P_{LT} &= -\tfrac{2M}{\alpha_{em}} \sqrt{\tfrac{q_{cm}^2}{Q^2}} \cdot G_E^p(Q^2) \cdot \beta_M(Q^2) + [P_{LT\ spin}] \end{aligned} \tag{3}$$

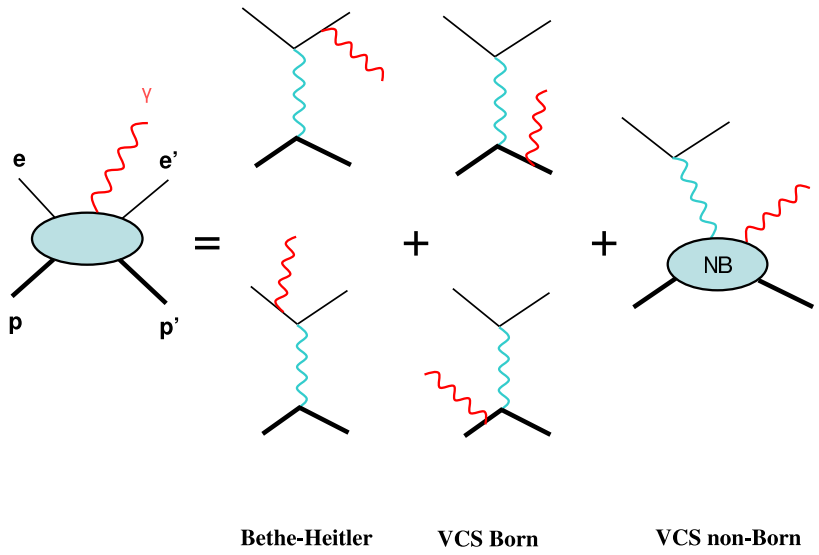

FIG. 2: The various contributions to the photon electroproduction amplitude.

where α_{em} is the fine structure constant and the terms in brackets are the spin part of the structure functions:

$$\begin{aligned} P_{TTspin} &= -3G_M^p(Q^2)\,\tfrac{q_{cm}^2}{\tilde{q}^0}\cdot(P^{(M1,M1)1}(Q^2) \\ &\quad -\sqrt{2}\,\tilde{q}^0\cdot P^{(L1,M2)1}(Q^2) \\ P_{LTspin} &= \tfrac{3}{2}\,\tfrac{q_{cm}\sqrt{Q^2}}{\tilde{q}^0}G_M^p(Q^2)\cdot P^{(L1,L1)1}(Q^2) \end{aligned} \tag{4}$$

where $\tilde{q}^0$ is the CM energy of the virtual photon in the limit $q'_{cm} \to 0$. One can note that P_{LL} is proportional to the electric GP, and the scalar part of P_{LT} is proportional to the magnetic GP. Using this LET approach one cannot extract all six dipole GPs separately from an unpolarised experiment since only three independent structure functions appear and can be extracted assuming the validity of the truncation to $\mathcal{O}(q'^2_{cm})$. Furthermore in order to isolate the scalar part in these structure functions a model input is also required.

However, since the sensitivity of the VCS cross sections to the GPs grows with the photon energy it is advantageous to go to higher photon energies. Above the pion threshold the VCS amplitude becomes complex. While T^{BH} and T^{Born} remain real, the amplitude $T^{Non-Born}$ acquires an imaginary part, due to the coupling to the πN channel. The relatively small effect of GPs below the pion threshold, which is contained in $d\sigma_{Non-Born}$, becomes more important in the region above the pion threshold and up to the $\Delta(1232)$ resonance, where the LET does not hold. In this case a Dispersion Relations (DR) formalism is prerequisite to extract the polarizabilities in the energy region above pion threshold where the observables are generally more sensitive to GPs.

The Dispersion Relations (DR) formalism developed by B.Pasquini et al. [5, 6] for RCS and VCS allows the extraction of structure functions and GPs from photon electroproduction experiments. The calculation provides a rigorous treatment of the higher-order terms in the VCS amplitude, up to the $N\pi\pi$ threshold, by including resonances in the πN channel. The Compton tensor is parameterised through twelve invariant amplitudes $F_i (i = 1, 12)$. The GPs are expressed in terms of the

non-Born part F_i^{NB} of these amplitudes at the point $t = -Q^2, \nu = (s-u)/4M = 0$, where s, t, u are the Mandelstam variables of the Compton scattering. All of the F_i^{NB} amplitudes, with the exception of two, fulfill unsubtracted dispersion relations. These s-channel dispersive integrals are calculated through unitarity. They are limited to the πN intermediate states, which are considered to be the dominant contribution for describing VCS up to the $\Delta(1232)$ resonance region. The calculation uses pion photo- and electroproduction multipoles [7] in which both resonant and non-resonant production mechanisms are included. The amplitudes F_1 and F_5 have an unconstrained part beyond the πN dispersive integral. Such a remainder is also considered for F_2. For F_5 this asymptotic contribution is dominated by the t-channel π^0 exchange, and with this input all four spin GPs are fixed. For F_1 and F_2, an important feature is that in the limit $(t = -Q^2, \nu = 0)$ their non-Born part is proportional to the GPs β_M and $(\alpha_E + \beta_M)$, respectively. The remainder of $F_{1,2}^{NB}$ is estimated by an energy-independent function, noted $\Delta\beta$ and $\Delta(\alpha+\beta)$ respectively. This term parameterises the asymptotic contribution and/or dispersive contributions beyond πN. For the magnetic GP one gets:

$$\begin{aligned} \beta_M(Q^2) &= \beta^{\pi N}(Q^2) + \Delta\beta \\ \Delta\beta &= \frac{[\beta^{exp} - \beta^{\pi N}]_{Q^2=0}}{(1+Q^2/\Lambda_\beta^2)^2} \ . \end{aligned} \tag{5}$$

The sum $(\alpha_E + \beta_M)$ follows a similar decomposition, and thus the electric GP too:

$$\begin{aligned} \alpha_E(Q^2) &= \alpha^{\pi N}(Q^2) + \Delta\alpha \\ \Delta\alpha &= \frac{[\alpha^{exp} - \alpha^{\pi N}]_{Q^2=0}}{(1+Q^2/\Lambda_\alpha^2)^2} \ . \end{aligned} \tag{6}$$

The two scalar GPs are not fixed by the model, and their unconstrained part is parametrised by a dipole form, as given by eqs.(5,6). This dipole form is arbitrary while the mass parameters Λ_α and Λ_β only play the role of intermediate quantities in order to extract VCS observables. In the DR calculation Λ_α and Λ_β are treated as free parameters, which can furthermore vary with Q^2. Their value can be adjusted by a fit to the experimental cross section, separately at each Q^2. Then the calculation is fully constrained and provides all VCS observables, the scalar GPs as well as the structure functions, at this Q^2.

C. The experimental and theoretical landscape of the GPs

A series of VCS experiments performed in the past decade at MAMI [8, 9], JLab [10, 11] and Bates [12] have provided a first experimental exploration of the electric and magnetic GPs of the proton. These experiments involve measurements both below and above the pion threshold, and results have been extracted both within the LEX and the DR approach. These results have illustrated a very nice agreement between the LEX and the DR extracted values for the Generalized Polarizabilities. Furthermore, the consistency of the DR extracted measurements has been exhibited for measurements both below and above the pion threshold, and up to the first resonance region [10, 11]. These measurements have also highlighted the expected enhanced sensitivity to the GPs as one measures in the resonance region.

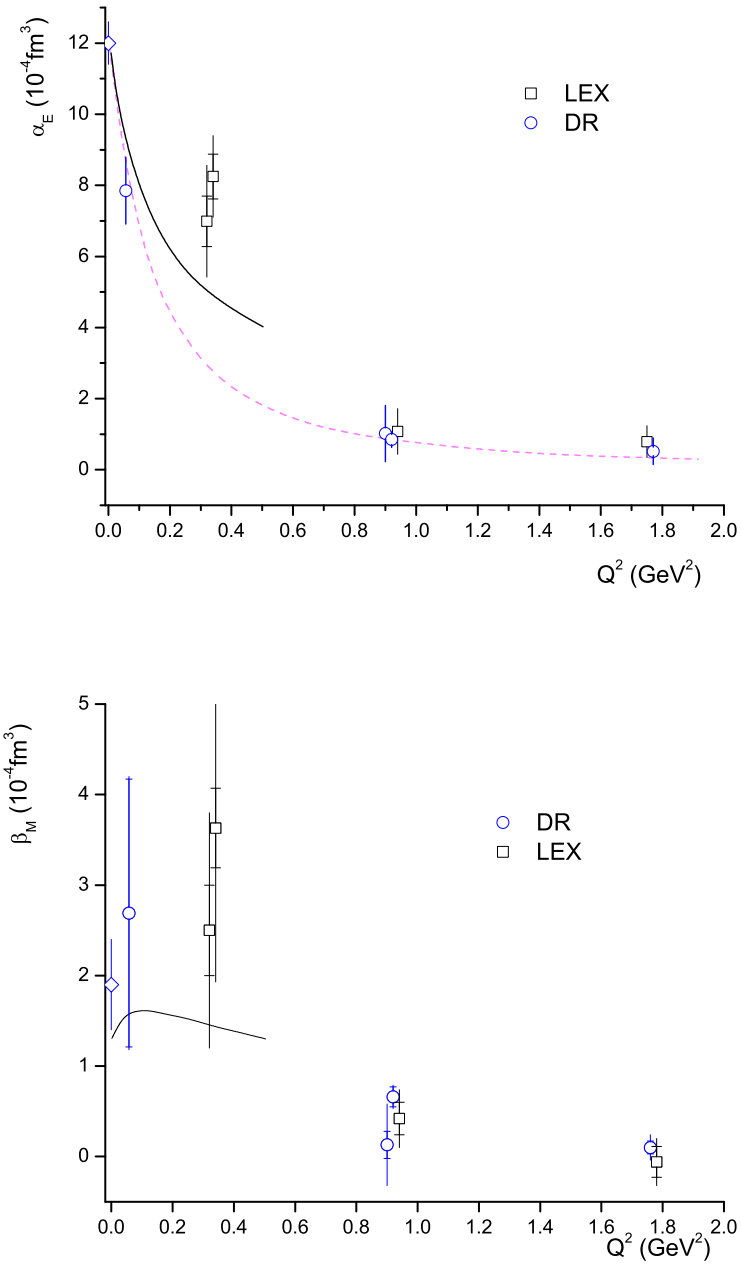

FIG. 3: World data [8–12] on the electric GP α_E (top panel) and the magnetic GP β_M (bottom panel). Open circles correspond GPs extracted through DR while the open boxes through LEX. The solid curve corresponds to HBChPT [17, 18]. The dipole fall off of α_E (dashed line) from the DR calculation [5, 6] is able to describe all world data except the MAMI measurements.

In Fig. 3 one can see the extracted electric and magnetic GPs from the above experiments. The first experimental evidence clearly contradict the naive Ansatz of a single-dipole fall-off for α_E as a function of Q^2; the data point out to an enhancement at low Q^2 evidenced by the MAMI measurements [8, 9], where two independent experiments at this Q^2 were able to confirm the same measurement for α_E. This unexpected structure is currently not understood and a variety of processes are candidates to explain this behavior (such as the mesonic cloud effects). Investigating the unexpected behavior of

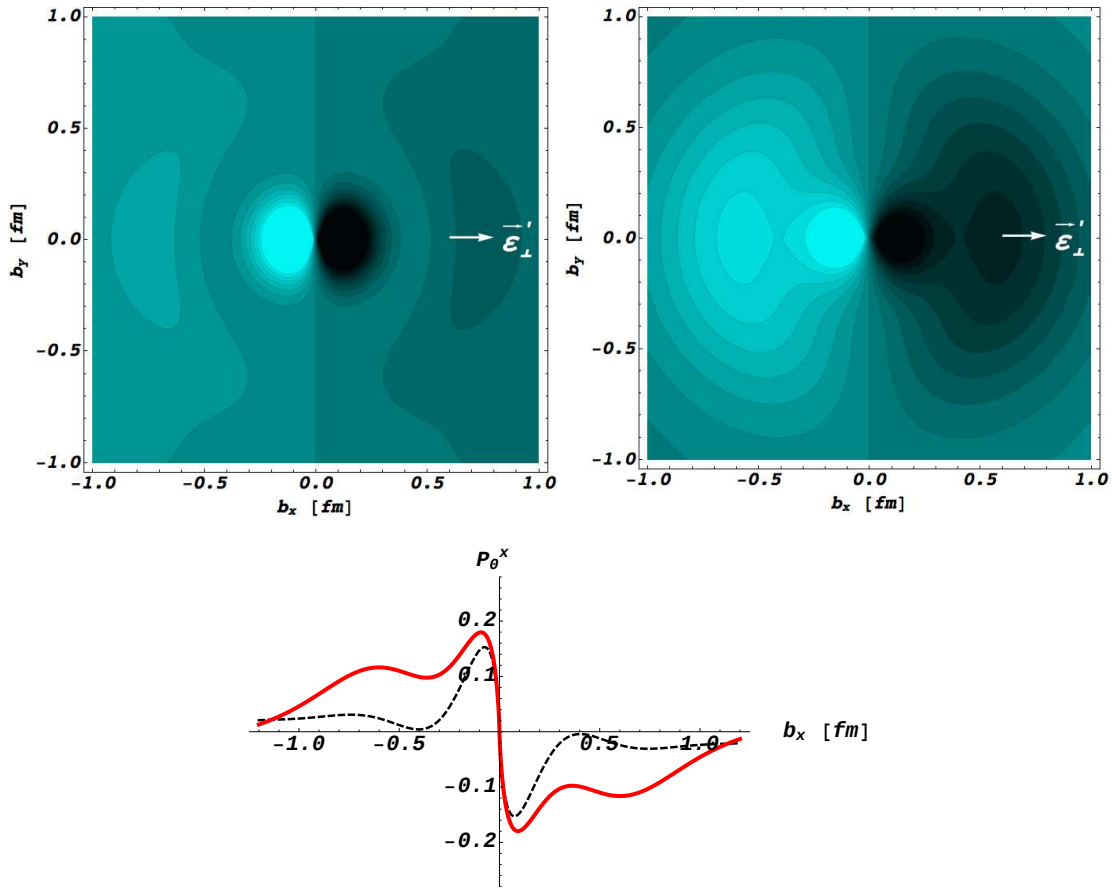

FIG. 4: Figure from [30]. Induced polarization, P_0^x, in a proton of definite light-cone helicity, when submitted to an e.m. field with photon polarization along the x-axis, as indicated. Top left (top right) panel is for GP I (GP II), see text. The light (dark) regions correspond to the largest (smallest) values. The lower panel compares P_0^x along $b_y = 0$: dotted curve is for GP I; solid curve is for GP II.

α_E represents an excellent opportunity to gain a deeper insight to the structure and the dynamics of the nucleon. This can be achieved with more precise measurements and a detailed mapping of α_E as a function of Q^2. As far as the magnetic GP is concerned it's value is smaller than the electric GP, as expected; that makes it more difficult to measure, as the β_M value is more sensitive to the experimental errors. Being able to achieve a more precise exploration of the magnetic polarizability can offer mainly a better understanding of the processes manifesting in the interplay between diamagnetism and paramagnetism in the proton. Currently there is an ongoing effort at MAMI to further explore the generalized polarizabilities in the region below $Q^2 = 0.5\ (GeV/c)^2$. This exploration involves a set of measurements below the pion threshold [13] as well as a set of measurements above the pion threshold and up to the $\Delta(1232)$ resonance region [14]. Both of the experiments have acquired data and are currently in the data analysis phase; the precision of these measurements is expected to be competitive to the previous MAMI measurements at $Q^2 = 0.33\ (GeV/c)^2$. Nevertheless, in order to achieve a complete picture for the GPs high precision measurements have to be provided also above the kinematical range that MAMI can currently access; these measurements should aim to bridge the kinematical range currently being explored at MAMI and the GPs measurements previously performed at JLab at high Q^2 [10, 11].

The GPs have been calculated by a variety of theoretical approaches. It has to be pointed out that none of the theoretical calculations is able to describe the observed structure of α_E around the MAMI measurement, as they all predict a smooth fall-off as a function of Q^2. In heavy baryon

chiral perturbation theory (HBChPT) the polarizabilities are pure one-loop effects to leading order in the chiral expansion [15], emphasizing the role of the pion cloud; the scalar GPs have been calculated to order p^3 [16–18], while the spin GPs have been calculated to order p^4 [19, 20]. The first nucleon resonance $\Delta(1232)$ is taken into account either by local counterterms (ChPT, [15]) or as an explicit degree of freedom (small scale expansion SSE of [18]). In non-relativistic quark constituent models [1, 21–23] the GPs involve the summed contribution of all nucleon resonances but do not embody a direct pionic effect. The calculation of the linear-σ model [24, 25] involves all fundamental symmetries but does not include the Δ resonance, while the effective lagrangian model [26] includes resonances and the pion cloud in a more phenomenological way. A calculation of the electric GP was made in the Skyrme model [27]. Lattice calculations are for the moment limited to polarizabilities in RCS [28] but significant progress on that front is expected in the next few years.

Most recently the developed formalism to extract light-front quark charge densities from nucleon form factor data was extended to the deformations of these quark charge densities when applying an external electric field [29, 30] which in turn allows for the concept of GPs to be used to describe the spatial deformation of the charge and magnetization densities in such a case. The induced polarization in a proton when submitted to an e.m. field is presented in Fig. 4, where two parametrizations (GP I and GP II) have been considered for the electric GP [31]. GP I corresponds to a fit of α_E to the MIT-Bates and JLab data and leads to a dipole fall-off of α_E. However this parametrization does not describe the MAMI data which indicate an additional structure at intermediate Q^2. A good description of all available data is obtained by parameterization GP II consisting of a sum of a dipole and a gaussian. One clearly sees that the enhancement at intermediate Q^2 in the electric GP (GP II) as compared with GP I, yields a spatial distribution of the induced polarization that extends noticeably to larger transverse distances. High precison VCS experiments, that will allow to pin down more precisely the behavior of the GPs at intermediate Q^2 values, will be able to verify, with greater precision, this large distance structure.

II. THE EXPERIMENT

A. The experimental setup

The experiment will utilize standard Hall C equipment to provide measurements of the Generalized Polarizabilities of the proton in Virtual Compton Scattering. The SHMS and HMS spectrometers [32, 33] will be used to detect electrons and protons in coincidence respectively, while the reconstructed missing mass will provide the identification of the photon. An electron beam of $E_\circ = 4400\ MeV$ and $I = 85\mu$A, as well as a 15 cm long liquid hydrogen target will also be required for this measurement.

The experiment will explore the GPs within the range of $Q^2 = 0.4\ (GeV/c)^2$ to $Q^2 = 0.75\ (GeV/c)^2$ in order to investigate the non trivial structure of α_E at the low and medium momentum transfer region, as well as to offer a precise measurement of β_M. The sensitivity to the polarizabilities is increased as one measures Compton scattering observables above the pion threshold and into the $\Delta(1232)$ resonance region, which is the region that this experiment will explore. The kinematics of the experiment have been carefully selected to allow for the optimal extraction of the GPs. The VCS cross section measurements will be performed within a $\theta_{\gamma^*\gamma}$ range above $\approx 120^\circ$ for all kinematics, since below that range the BH process dominates the cross section (as shown in Fig. 6) and suppresses the sensitivity to the GPs. For every $\theta_{\gamma^*\gamma}$ setting measurements will be performed at $\phi_{\gamma^*\gamma} = 0^\circ$ and $\phi_{\gamma^*\gamma} = 180^\circ$ in order to also determine the in-plane azimuthal asymmetry of the VCS cross section with respect to the momentum transfer direction,

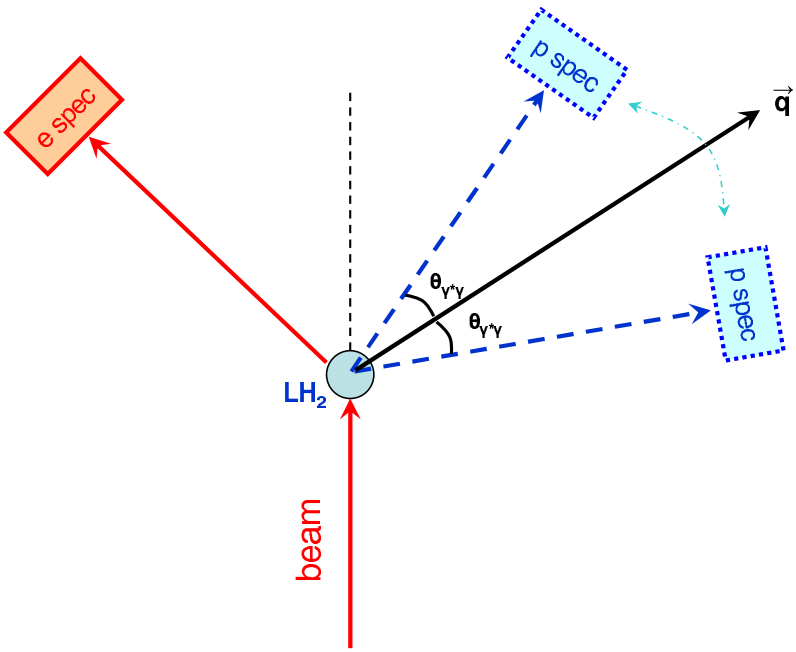

FIG. 5: Schematic representation of the experimental setup. The SHMS and the HMS spectrometers will be detecting electrons and protons respectively.

$$A_{(\phi_{\gamma^*\gamma}=0,\pi)} = \frac{\sigma_{\phi_{\gamma^*\gamma}=0} - \sigma_{\phi_{\gamma^*\gamma}=180}}{\sigma_{\phi_{\gamma^*\gamma}=0} + \sigma_{\phi_{\gamma^*\gamma}=180}}$$

which also exhibits sensitivity to the GPs. Measuring the asymmetry offers a certain number of advantages. Firstly, one can extract the polarizabilities without having to extract absolute cross sections. Furthermore, for a part of the $\theta_{\gamma^*\gamma}$ range of the measurements the sensitivity to the β_M practically cancels out in the asymmetry thus offering an additional advantage to the extraction of α_E. Finally, the fact that some of the systematic uncertainties of the cross sections are suppressed in the asymmetry allows for a more precise extraction of the GPs. A schematic representation of the experimental setup is presented in Fig. 5.

The possibility of performing this measurement in Hall A, using the two HRS spectrometers, has also been considered. It has been found that Hall C provides the ideal setup for this experiment. The HRS spectrometers have a lower angle limitation of 12.5° which effectively does not allow to perform the part I of the experiment with $E_\circ = 4400\ MeV$. One could re-adjust the kinematical settings to have the measurement done with a lower beam energy in Hall A but this will have a negative impact

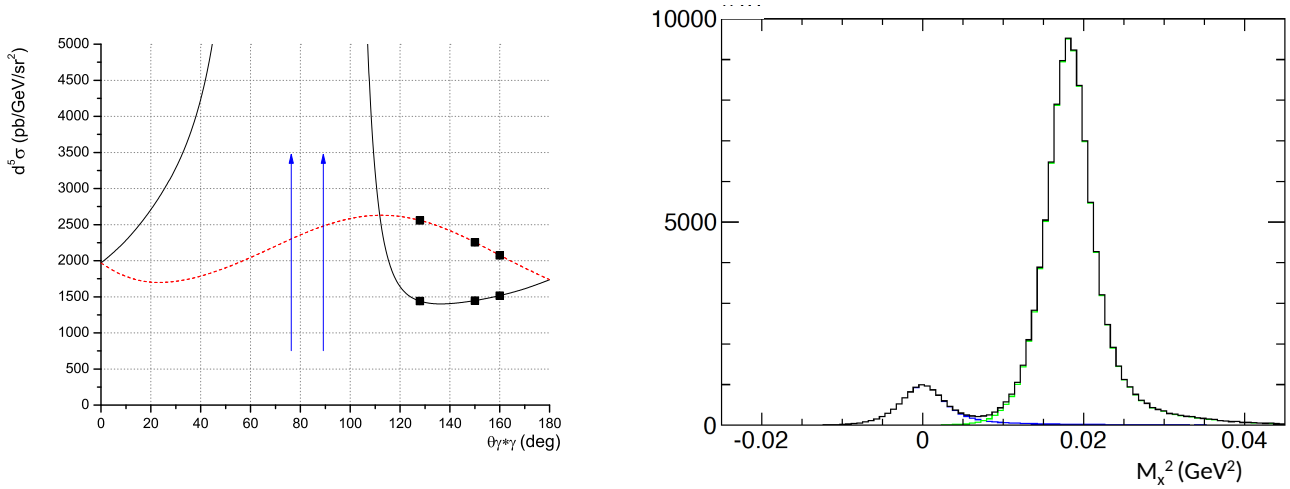

FIG. 6: Left panel: Projected cross sections at $Q^2 = 0.43\ (GeV/c)^2$. The solid and dashed curves correspond to cross sections at $\phi_{\gamma^*\gamma} = 0^\circ$ and 180°. The two arrows are pointing to the two BH peaks. Right panel: The reconstructed missing mass spectrum.

both to the sensitivity to the GPs as well as to the statistics of the measurement. For example, part I (see Table III) can run in Hall A with $E_\circ = 3300\ MeV$. For the same number of experiment days, the smaller cross section will result in smaller statistics that will increase the total uncertainty of α_E by $\approx 9\%$. At the same time the sensitivity of the measurement to α_E will be suppressed by $\approx 6.4\%$. As a result, the total uncertainty of α_E will increase by 16.5% compared to a measurement performed in Hall C (see Fig. 12), which nevertheless remains a very competitive measurement. A small advantage in this case is an improved resolution of the missing mass, since the HRS provides a better momentum resolution compared to the SHMS. If one wishes to run such a measurement with even lower beam energy of $E_\circ = 2200\ MeV$ (in order to allow the accelerator to provide simultaneously the maximum possible beam energy to another hall) then the statistical uncertainty will increase further while the sensitivity to the GPs will be reduced by $\approx$ 22%. Finally, it should be pointed out that, due to spectrometer constraints, the kinematical range of this experiment can not be accessed at MAMI, thus leaving JLab the only laboratory that could perform this measurement.

B. The experimental apparatus

The trigger will be a coincidence between the electrons in the SHMS and the protons in the HMS. The HMS will detect protons using the standard detector package. The protons can be identified by coincidence time-of-flight (TOF). At the momentum of 1 GeV/c, the proton, kaon and pion TOF will be 114, 91.2 and 82 ns for the 25 m HMS path length. An aerogel detector will not be necessary in the HMS detector stack. The combined proton and pion singles rates have been kept below 300kHz to be safe and have reliable tracking efficiency calculation. The total singles rates are presented in Table II. A study of tracking efficiency versus rate in the first scintillator plane, S1X, is plotted in Fig. 7. The new tracking efficiency algorithm would be used (green box points in the plot) and below 300 kHz the tracking efficiency is above 96% and smooth. Above 500 kHz the green points start to show scatter and thus these high rates should be avoided.

The SHMS will detect the electrons and use the standard detector package including the Noble Gas Cerenkov (NGC) which sits between the exit of the SHMS dipole and the first drift chamber (see

	Kinematical Setting	HMS singles rates (kHz)
Part I	Kin Ia	213
	Kin Ib	91
	Kin IIa	290
	Kin IIb	68
	Kin IIIa	300
	Kin IIIb	34
Part II	Kin IVa	102
	Kin IVb	37
	Kin Va	122
	Kin Vb	31
	Kin VIa	244
	Kin VIb	16

TABLE II: The combined proton and pion singles rates for the HMS spectrometer. All kinematical settings will run with I=85 μA except Kin IIIa that will run with I=45 μA.

Fig. 8). For this electron energy range , the NGC would be filled with Argon, since the pion threshold is at about 5.5 GeV/c. The NGC introduces extra multiple scattering (compared to running without it) which has been included in the Monte Carlo simulations. The combined electron and pion singles rates are below 160 kHz. The combination of the NGC and calorimeter will give an e:pion rejection ratio of 10,000:1. The drift chambers in the SHMS are similar to the HMS drift chambers and the tracking efficiency versus rate will be similar to Fig. 7.

Time will be needed to do luminosity scans to study target boiling, tracking efficiency and electronic deadtime. Conservatively, one day has been set aside for this in the run plan, but if other experiments are running the time would be shared with these experiments.

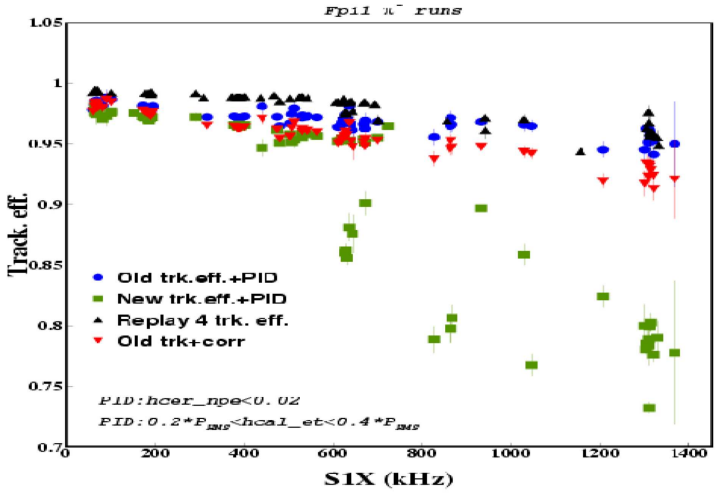

FIG. 7: Study of tracking efficiency versus rate in the first scintillator plane, S1X, of the HMS.

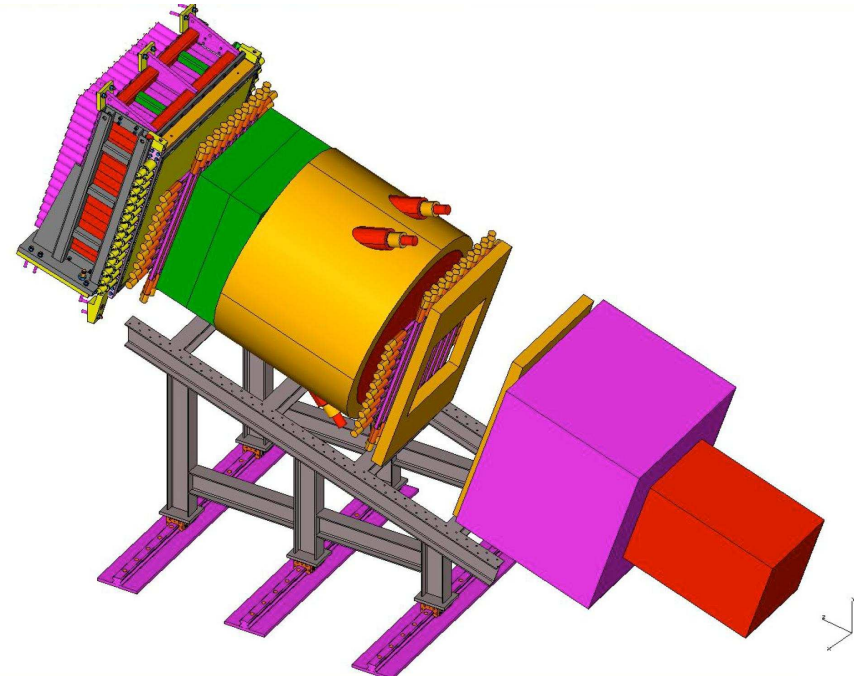

FIG. 8: The SHMS detector stack.

C. Kinematical settings and beam time request

The kinematical settings are summarized in Table III. They have been categorized in two groups, part I and part II, corresponding to measurements at a lower and at a higher Q^2. Monte-Carlo studies have been performed (see Fig. 9) for all of the proposed kinematics using SIMC [34]. The code includes the effects of offsets and finite resolutions while a physics model is averaged over the finite acceptances of the experimental apparatus. The reconstructed missing mass spectrum is presented in Fig. 6. For the calculation of the count rates and the beam time request the Dispersion Relations calculation [5] developed by B. Pasquini was used and folded over the experimental acceptance. The model has been proven very successful both in the calculation of the VCS cross sections above the pion threshold and in the extraction of the GPs [8–11, 35]. The beam time request per setting is summarized at the last column of Table III. The accidental rates have been calculated for all the kinematical settings. The proton and π^+ rates range between 10 kHz and 150 kHz, depending on the setting. The electron rates are 150 kHz and 40 kHz, for the two parts of the experiment respectively, while the π^- ones will only be at the order of a few kHz. All kinematical settings will run with I=85 μA except Kin IIIa that will run with I=45 μA in order to keep the HMS singles rates below 300 kHz. The coincidence signal to noise (S/N) ratios for a 1.2 ns timing window are summarized in Table III. The S/N ranges from ≈ 1 to 8, but for a quite wide missing mass cut of 70 MeV; a more tight missing mass applied during the analysis will be able to further improve the S/N ratio. Calibration data will be taken for normalization and calibration of the alignment of the spectrometers. Furthermore, the $p(e,e'p)\pi^\circ$ channel will be simultaneously measured, with high statistical precision, in every kinematical setting. Given the fact that the pion electroproduction cross section has been very precisely measured at the resonance region for the momentum transfer range of this experiment, these data will provide an additional normalization to all the kinematical settings of the experiment. It is also worth pointing out that throughout the experiment the beam energy will not vary, while there will only be one change of setting of the electron spectrometer,

	Kinematical Setting	$\theta_{\gamma^*\gamma}{}^\circ$	$\theta_e{}^\circ$	$P_e^{'}(MeV/c)$	$\theta_p{}^\circ$	$P_p^{'}(MeV/c)$	S/N	beam time (days)
Part I	Kin Ia	165	9.39	3820.5	40.85	1010.40	1.3	0.5
	Kin Ib	165	9.39	3820.5	48.45	1010.40	2.4	0.5
	Kin IIa	155	9.39	3820.5	38.34	995.20	1	0.5
	Kin IIb	155	9.39	3820.5	50.96	995.20	3.2	0.5
	Kin IIIa	128	9.39	3820.5	31.84	919.43	0.7	0.95
	Kin IIIb	128	9.39	3820.5	57.46	919.43	7.8	0.55
Part II	Kin IVa	165	11.54	3708.6	40.81	1175.25	2.6	1.5
	Kin IVb	165	11.54	3708.6	47.35	1175.25	5	2
	Kin Va	160	11.54	3708.6	39.73	1167.72	2.2	1.5
	Kin Vb	160	11.54	3708.6	48.43	1167.72	6.3	2
	Kin VIa	140	11.54	3708.6	35.52	1117.38	1.2	1.5
	Kin VIb	140	11.54	3708.6	52.64	1117.38	8	2

TABLE III: The kinematical settings of the proposed experiment. The S/N ratio involves a wide preliminary missing mass cut of 70 MeV; for the analysis a tighter missing mass cut will improve the S/N ratio even further. The beam time request per setting is presented in the last column of the table. A 4400 MeV beam, I=85 μA and a 15cm liquid hydrogen target are required for these measurements (Kin IIIa will run with I=45 μA in order to keep the HMS singles rates below 300 kHz).

going from part I of the experiment to part II. During part I, or part II, the electron arm angle and momentum will not change, while only the proton arm momentum and angle will be varied. This fact will provide an additional advantage to the system calibration as well as to the control of the systematic uncertainties.

The phase space covered by the 12 kinematical settings will allow the extraction of the GPs at $Q^2 = 0.43\ (GeV/c)^2$, $0.52\ (GeV/c)^2$, $0.65\ (GeV/c)^2$, and $0.75\ (GeV/c)^2$. The part I of the experiment will provide the two lowest Q^2 measurements, while part II will provide the two highest ones. The phase space for a pair of settings from part I (Kin Ia and Ib) and part II (Kin IVa and IVb) is presented in Fig. 9. With the requested beam time the cross sections will be measured with a statistical uncertainty ranging from $\pm$ 1% to $\pm$ 1.3%, depending on kinematics and the analysis bin. The systematic uncertainties will be the dominating factor, being at the order of $\approx \pm$ 3%. The uncertainty of the beam energy and of the scattering angle will introduce a systematic uncertainty to the cross section ranging from $\pm$ 1% to $\pm$ 2.5% depending on the kinematics. Other sources of systematic uncertainties involve the target density, detector efficiency, acceptance, and target cell background; each one of these contributes $\pm$ 0.5% to the uncertainty. Systematic uncertainties related to the target length, beam charge, dead time corrections, and contamination of pions under the photon peak will contribute $\pm$ 0.3% each. The uncertainty due to the radiative corrections will be $\pm$ 1.5%. Finally, for a more conservative approach to the systematic uncertainties a $\pm$ 0.5% contribution has been assigned to other corrections. For the asymmetries the systematic uncertainties are still larger compared to the statistical ones, but not as dominant as in the case of the cross sections, and are expected to be at the order of $\approx$ 1.1% (in absolute asymmetry magnitude). The extraction of the Generalized polarizabilities will be performed in a straightforward way through a fit to the measured cross sections and asymmetries, as was done in previous measurements [10, 11]. The mass scale parameters Λ_α and Λ_β will be fitted by a χ^2 minimization which compares the DR cross sections and asymmetries to the measured ones, and the two scalar GPs will be

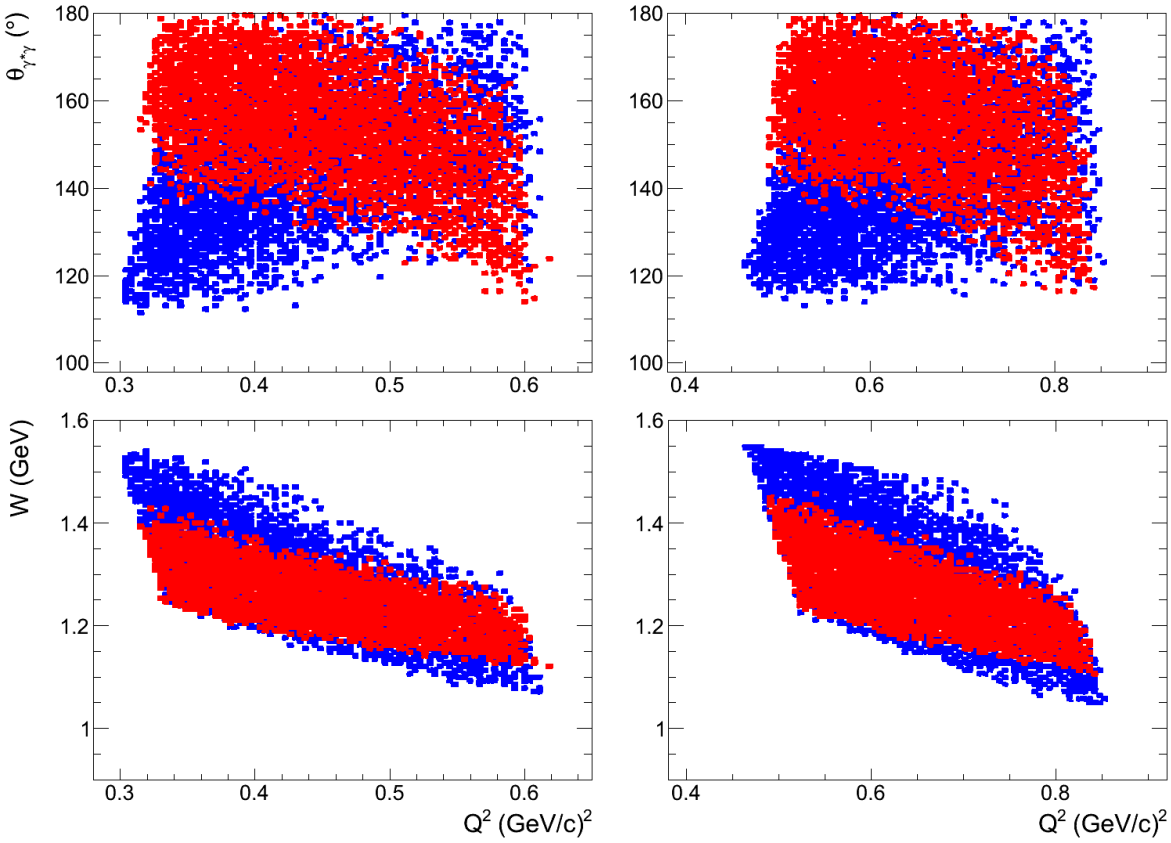

FIG. 9: Correlation of the phase space variables for a pair of $\phi_{\gamma^*\gamma} = 0^\circ$, 180° measurements, with the two different colors corresponding to $\phi_{\gamma^*\gamma} = 0^\circ$ and 180° respectively. Left (top and bottom) and right (top and bottom) correspond to settings from part I and part II, respectively.

determined. The primary source of uncertainty for both the electric and the magnetic GP will be the systematic uncertainties, with the statistical uncertainties being, for both GPs, $\approx$ 70% compared to the systematic ones, for all the kinematical settings. Finally, there is a third source of uncertainty to the determination of the GPs that has been taken into account. This involves the knowledge of the proton elastic and transition form factors, which are very well known in this kinematic range but not with an infinite precision, as well as the set of multipoles for pion electroproduction utilized in the DR calculation. Various parametrizations for the form factors as well as different multipole sets have been applied, and their effects to the determination of the scalar GPs have been quantified. Then all of these uncertainties have been added in quadrature. The total uncertainty has been calculated to be comparable (nearly equal) to the total effect of the experimental systematic uncertainties.

In Fig. 10 the projected cross sections and asymmetries are presented for $Q^2 = 0.65\ (GeV/c)^2$. The solid (red) and dashed (blue) curves correspond to a variation to the electric GP from $\alpha_E = 4.8\ 10^{-4}\ fm^3$ ($\beta_M = 1.1\ 10^{-4}\ fm^3$) to $\alpha_E = 1.5\ 10^{-4}\ fm^3$ ($\beta_M = 1.1\ 10^{-4}\ fm^3$). A variation of β_M from $= 0.4\ 10^{-4}\ fm^3$ to $= 1.6\ 10^{-4}\ fm^3$ is presented through the two, dotted and dash-dot, orange curves at the cross section figures. The same variation in β_M is represented through the light blue band in the asymmetry figure, at the bottom panel of the figure. One can observe that above $\theta_{\gamma^*\gamma} \approx 160^\circ$ the variation to the β_M is affecting in a systematically similar way both cross sections and this is reflected as a cancelation of the effect in the asymmetry (supression of the light

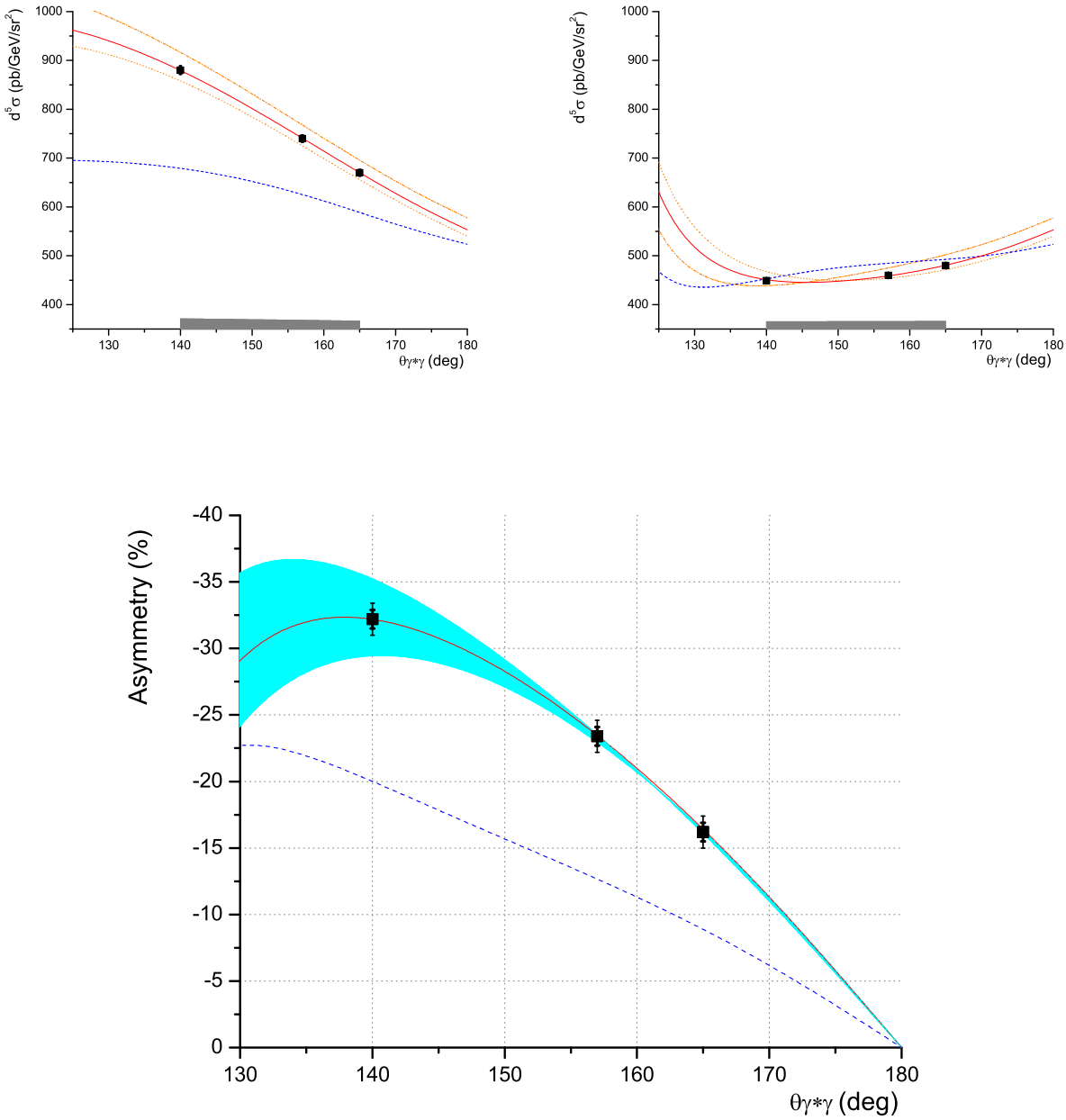

FIG. 10: Projected cross sections (top panel) and asymmetries (bottom panel) at $Q^2 = 0.65\ (GeV/c)^2$. Solid red (dashed blue) curve corresponds to $\alpha_E = 4.8\ 10^{-4}\ fm^3$, $\beta_M = 1.1\ 10^{-4}\ fm^3$ ($\alpha_E = 1.5\ 10^{-4}\ fm^3$, $\beta_M = 1.1\ 10^{-4}\ fm^3$). A variation of β_M from $= 0.4\ 10^{-4}\ fm^3$ to $= 1.6\ 10^{-4}\ fm^3$ is presented through the two orange curves (dotted, dash-dot) at the top panel. The same variation in β_M is given through the light blue band in the asymmetry at the bottom panel

blue band in the corresponding $\theta_{\gamma^*\gamma}$ range). In Fig. 11 the projected asymmetries are presented for $Q^2 = 0.43\ (GeV/c)^2$ and a similar variation to the two scalar GPs is also presented. The projected measurements for α_E and β_M are presented in Fig. 12 and Fig. 13, respectively. The inner error bar corresponds to the statistical uncertainty and the outer one corresponds to the total uncertainty of the measurement. The experiment can provide a high precision measurement of both scalar GPs. It will allow to explore the non trivial structure of α_E at the low and medium momentum

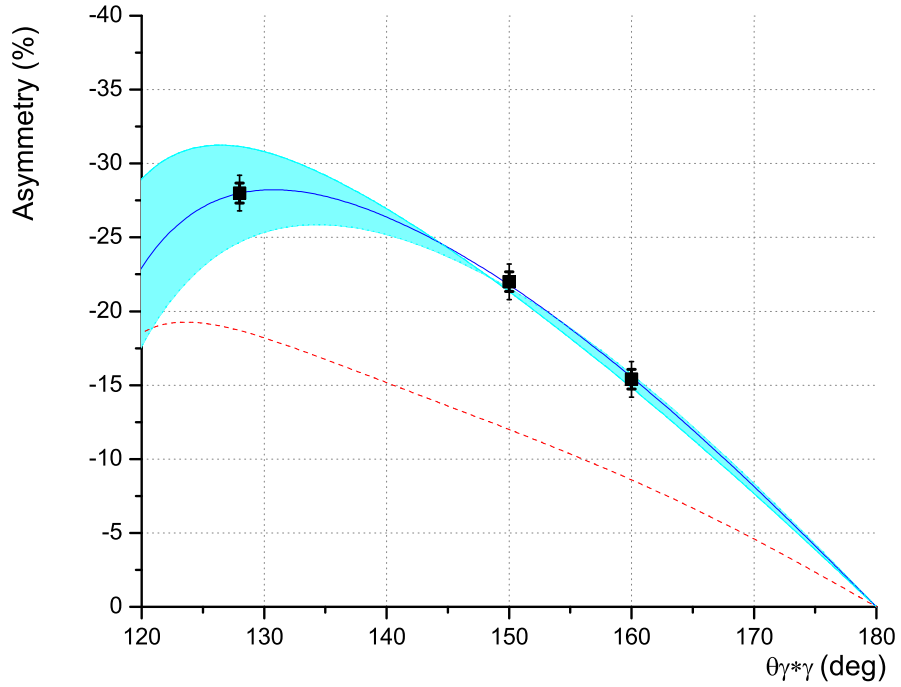

FIG. 11: Projected asymmetries at $Q^2 = 0.43\ (GeV/c)^2$. The solid (dashed) curve corresponds to $\alpha_E = 5.8\ 10^{-4}\ fm^3$, $\beta_M = 1.6\ 10^{-4}\ fm^3$ ($\alpha_E = 2.4\ 10^{-4}\ fm^3$, $\beta_M = 1.6\ 10^{-4}\ fm^3$). The light blue band corresponds to a variation of β_M from $= 0.6\ 10^{-4}\ fm^3$ to $= 2.5\ 10^{-4}\ fm^3$.

transfer region in order to be able to decode the underlying nucleon dynamics. The knowledge of the magnetic GP will also be greatly improved by the proposed measurements. Finally, it is also worth emphasizing that the two lowest in Q^2 data points (corresponding to part I of the experiment), which by themselves will be a significant advance to our knowledge of the two polarizabilities, will only require 3.5 days of beam time.

III. SUMMARY

We propose to conduct a measurement of the Virtual Compton Scattering reaction in Hall C, using the HMS and SHMS spectrometers, that will allow the extraction of the two scalar Generalized Polarizabilities of the proton in the region of $Q^2 = 0.4\ (GeV/c)^2$ to $Q^2 = 0.75\ (GeV/c)^2$. The unique capabilities of Hall C, namely the high resolution of the spectrometers combined with the ability to place the spectrometers in small angles, will allow high precision measurements of both α_E and β_M. The Generalized Polarizabilities are fundamental quantities of the nucleon, sensitive to both the role of the quark and pion degrees of freedom and as such they are extremely valuable for a deeper and more complete understanding of the nucleon structure. The proposed measurements will greatly advance our current knowledge of both α_E and β_M and will contribute in a valuable way to our understanding of the nucleon dynamics. **We request for a $E_\circ = 4400 MeV$ beam at I=85 μA, a 15 cm liquid hydrogen target and a total of 14 days of beam on target for the proposed experiment**. An additional one day will be required for calibration runs, but if this experiment is running along with a group of other experiments the time would be shared with

these experiments. Finally, this measurement could also take place in Hall A, as described earlier in the experimental setup section, using the two HRS spectrometers and two different beam energy settings of $E_\circ = 3300 MeV$ and $E_\circ = 4400 MeV$.

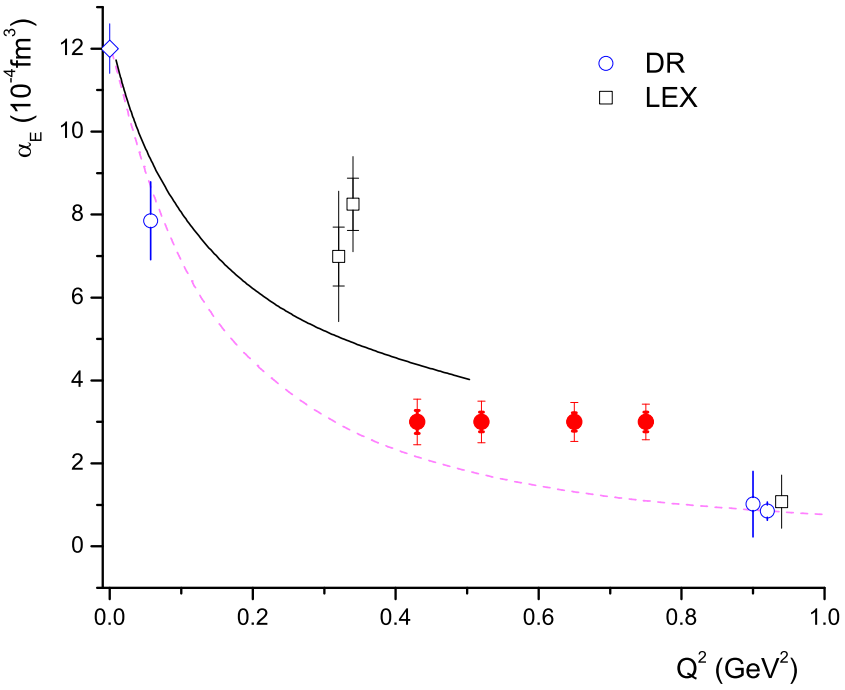

FIG. 12: The projected measurements for α_E (solid circles). The inner error bar corresponds to the statistical uncertainty and the outer one corresponds to the total uncertainty of the measurement. References for the world data and curves are given in the caption of Fig. 3.

[1] P.A.M. Guichon, G.Q. Liu and A.W. Thomas, Nucl. Phys. A 591 (1995) 606.
[2] D. Drechsel, G. Knochlein, A.Y. Korchin, A. Metz, S. Scherer, Phys. Rev. C 57, 941 (1998)
[3] D. Drechsel, G. Knochlein, A.Y. Korchin, A. Metz, S. Scherer, Phys. Rev. C 58, 1751 (1998)
[4] V. Olmos de Leon, et al., Eur. Phys. J. A10 (2001) 207
[5] B. Pasquini, M. Gorchtein, D. Drechsel, A. Metz, M. Vanderhaeghen, Eur. Phys. J. A11 (2001) 185-208.
[6] D. Drechsel, B. Pasquini, M. Vanderhaeghen, Phys. Rept. 378 (2003) 99-205.
[7] D. Drechsel, O. Hanstein, S.S. Kamalov, L. Tiator, Nucl. Phys. A 645, 145 (1999)
[8] J. Roche, et al., Phys. Rev. Lett. 85 (2000) 708-711.
[9] P. Janssens, et al., Eur. Phys. J. A37 (2008) 1-8
[10] G. Laveissiere, et al., Phys. Rev. Lett. 93 (2004) 122001
[11] H. Fonvieille, et al., Phys. Rev. C86 (2012) 015210
[12] P. Bourgeois, et al., Phys. Rev. Lett. 97 (2006) 212001
[13] MAMI experiment A1/1-09, H. Fonvieille et al, *A study of the Q^2-dependence of the structure functions $P_{LL} - P_{TT}/\epsilon$ and P_{LT} and the generalized polarizabilities α_E and β_M in Virtual Compton Scattering at MAMI.*
[14] MAMI experiment A1/3-12, N. Sparveris et al, *Study of the nucleon structure by Virtual Compton Scattering measurements at the Δ resonance.*
[15] V. Bernard, N. Kaiser, A. Schmidt, U.G. Meissner, Phys. Lett. B 319, 269 (1993) and references therein
[16] T. R. Hemmert, B. R. Holstein, G. Knochlein, S. Scherer, Phys. Rev. D55 (1997) 2630-2643.
[17] T. R. Hemmert, B. R. Holstein, G. Knochlein, S. Scherer, Phys. Rev. Lett. 79 (1997) 22-25.
[18] T. R. Hemmert, B. R. Holstein, G. Knochlein, D. Drechsel, Phys. Rev. D62 (2000) 014013.
[19] C. W. Kao, M. Vanderhaeghen, Phys. Rev. Lett. 89 (2002) 272002.

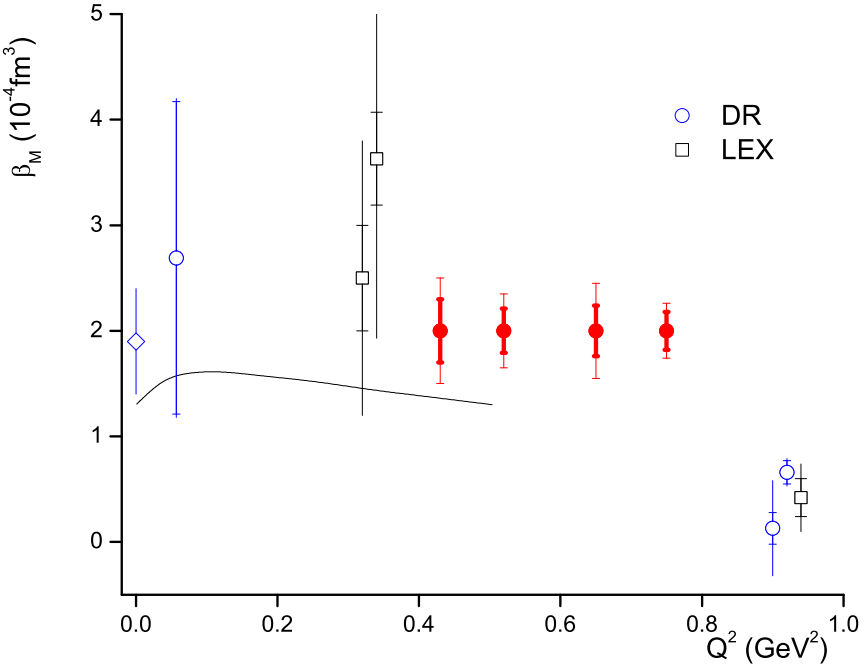

FIG. 13: The projected measurements for β_M (solid circles). The inner error bar corresponds to the statistical uncertainty and the outer one corresponds to the total uncertainty of the measurement. References for the world data are given in the caption of Fig. 3.

[20] C.-W. Kao, B. Pasquini, M. Vanderhaeghen, Phys. Rev. D70 (2004) 114004.
[21] G. Q. Liu, A. W. Thomas, P. A. M. Guichon, Austral. J. Phys. 49 (1996) 905-918.
[22] B. Pasquini, S. Scherer, D. Drechsel, Phys. Rev. C63 (2001) 025205.
[23] B. Pasquini, G. Salme, Phys. Rev. C57 (1998) 2589.
[24] A. Metz, D. Drechsel, Z. Phys. A356 (1996) 351-357.
[25] A. Metz, D. Drechsel, Z. Phys. A359 (1997) 165-172.
[26] M. Vanderhaeghen, Phys. Lett. B368 (1996) 13-19.
[27] M. Kim, D.-P. Min (1997) [hep-ph/9704381]
[28] W. Detmold, B. Tiburzi, A. Walker-Loud, Phys. Rev. D 81, 054502 (2010)
[29] A.I. Lvov, S. Scherer, B. Pasquini, C. Unkmeir, D. Drechsel, Phys. Rev. C 64, 015203 (2001)
[30] M. Gorchtein, C. Lorce, B. Pasquini, M. Vanderhaeghen, Phys. Rev. Lett. 104, 112001 (2010)
[31] B. Pasquini, D. Drechsel, and M. Vanderhaeghen, Eur. Phys. J. Special Topics 198, 269285 (2011)
[32] https://www.jlab.org/Hall-C/upgrade/
[33] https://www.jlab.org/Hall-C/equipment/HMS.html
[34] https://hallcweb.jlab.org/wiki/index.php/Monte_Carlo
[35] N. Sparveris et al, Phys. Rev. C 78, 025209 (2008)